Journal of ELECTRONIC MATERIALS, Vol. 48, No. 2, 2019
https://doi.org/10.1007/s11664-018-6791-7
© 2018 The Minerals, Metals & Materials Society

X-ray Diffraction Line Profile Analysis of Undoped and Se-Doped SnS Thin Films Using Scherrer's, Williamson–Hall and Size–Strain Plot Methods

HOSEIN KAFASHAN[1,2,3]

1.—Department of Materials Science and Engineering, Ahvaz Branch, Islamic Azad University, Ahvaz, Iran. 2.—e-mail: hosein840521@gmail.com. 3.—e-mail: hosein.kafashan@iauahvaz.ac.ir

An electrochemical route has been employed to prepare undoped and Se-doped SnS thin films. Six samples including undoped and Se-doped SnS thin films were deposited on the fluorine-doped tin oxide glass substrate. An aqueous solution containing 2 mM $SnCl_2$ and 16 mM $Na_2S_2O_3$ was used in the electrolyte. Different Se-doped SnS samples were prepared by adding the various amounts of 4 mM SeO_2 solution into the electrolyte. The applied potential (E), time of deposition process (t), pH, and bath temperature (T) were kept at − 1 V, 30 min, 2.1, and 60°C, respectively. After the completion of the deposition process, x-ray diffraction (XRD) and transmission electron microscopy (TEM) were utilized to characterize the deposited thin films. XRD patterns clearly showed that the synthesized undoped and Se-doped SnS thin films were crystallized in the orthorhombic structure. Using Scherrer's method, the crystallite size of deposited thin films is calculated. In addition, the crystallite size and lattice strain have been estimated using the modified form of the Williamson–Hall (W–H) method containing a uniform deformation model, a uniform deformation stress model, a uniform deformation energy density model, and by the size–strain plot method (SSP). The shape of SnS crystals was spherical in TEM images. The results showed that there was a good agreement in the particle size obtained from the W–H method and the SSP method with TEM images.

Key words: Line profile analysis, Se-doped SnS, Williamson–Hall method, size–strain plot method, thin films

INTRODUCTION

The mechanical behavior of micro/nano sized materials varies with their bulk, and it is known that "smaller is stronger". Up to now, electron microscopy was used to investigate the small-scale mechanics of materials based on *ex situ* and *in situ* characterization. The limitation of electron microscopy techniques is *2D* projection of a surface from thin foil of material. In the last two decades, a great development was reached at *3rd* generation synchrotrons that hard x-ray beams can focus down to the 100-nm scale.[1] A synchrotron is a particle accelerator, which can convert the energy of the fast moving electrons into a high-energy white x-ray beam.[2] The power of this method as a local stress probe for micro- and nanoscale devices is the measurement of stresses at submicron resolution, the measurement of the deviatoric components of the stresses, and the measurement of hydrostatic components of the stress tensors.[3] Synchrotron x-ray diffraction methods containing x-ray absorption spectroscopy (XAS), x-ray diffraction (XRD), pair distribution function (PDF) and x-ray scattering,[4] can deliver structural properties of materials with high resolution and fully *3D*.[1]

(Received November 2, 2017; accepted November 3, 2018; published online November 19, 2018)

Today, researchers focused on the IV–VI group semiconductors that have attracted great attention owing to their narrow band gap energy (E_g), and capability of their use in photovoltaic devices, near-infrared detectors, biomedical applications, and solar cell devices.[5] Among these IV–VI group semiconductors, tin mono-sulfide (SnS) is a promising candidate material for future energy sources due to the easy availability and low cost of the constituent elements (Sn and S), and it has good optical properties.[6] Compared to the other compounds containing rare metals (In and Ga) such as $Cu(In,Ga)(S,Se)_2$ (CIGS) or $Cu_2ZnSn(S,Se)_4$ (CZTS), SnS is a favorable semiconductor due to low material cost and simple material system.[7] SnS has p-type conductivity.[8] Due to appropriate band gap ($E_g \sim 1.3$ eV),[9,10] high absorption properties ($\alpha > 10^4$ cm^{-1}),[11] high carrier concentration (p 10^{15}–10^{18} cm^{-3}),[12] and high mobility (hole mobility ~ 90 cm^2 V^{-1} s^{-1}),[13] SnS can be used as a photovoltaic absorber layer, photoelectrochemical cell, Li-ion battery anodes, electrochemical capacitors, and photodetectors.[13] SnS crystallizes in orthorhombic structure with the lattice parameters of a = 0.43291 nm, b = 1.11923 nm (long b-axis) and c = 0.39838 nm (JCPDS card no 39-0354). It also has a deformed NaCl structure. The coordination number of the Sn atom is six, containing three short Sn-S bonds within the layer and three long bonds between the layers, as shown in Fig. 1.[7] The layers are weakly held together by Van der Waals forces. The interlayer is vulnerable to the penetration of impurities.[14]

There are many methods to produce SnS thin films such as thermal evaporation,[15–17] electron-beam evaporation,[18] spray pyrolysis,[6,19–21] spin coating,[22] electrodeposition,[23–27] chemical bath deposition (CBD),[28–31] sputtering,[32] liquid phase deposition,[12] chemical vapor deposition (CVD),[33] solvothermal method,[34] and a two-stage process.[35] Among these techniques, electrodeposition technique was more suitable due to simplicity, low cost, and the facility of controlling the parameters with high accuracy. In addition, the electrodeposition method does not need a vacuum[36,37].

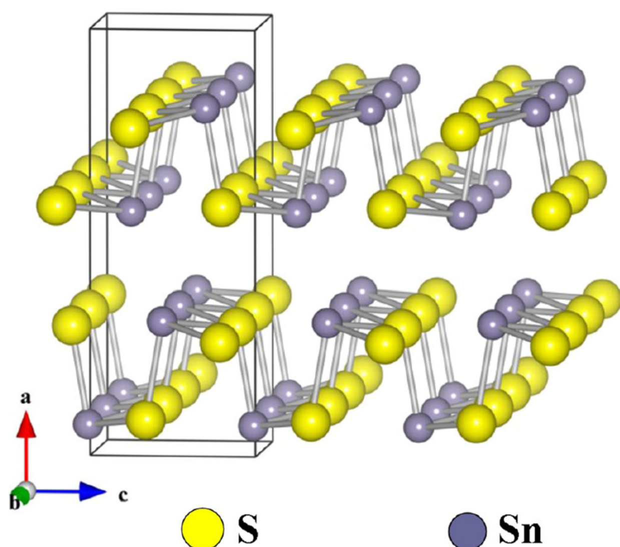

Fig. 1. The arrangement of Sn and S in the SnS lattice[35] (reproduced with permission from ACS Publications).

As the study of statistical quantities of dislocation densities is very time consuming via TEM, the investigation of dislocation loops in irradiated materials was restricted using TEM analysis. Diffraction peak profile analysis (DPPA) is a very useful method to investigate the dislocation structure, dislocation density, and population distribution in the mechanically deformed materials. Therefore, DPPA was a complementary method to TEM study.[38,39] The prevailing active slip-systems can be investigated using high-resolution x-ray line profile analysis.[40] The convolutional multiple whole profile (CMWP) technique can estimate the dislocation densities, the prevailing active slip-systems, and the subgrain size. Z. Fan et al. investigated the dislocation densities and slip activities in the deformed Zr and its alloys using x-ray or neutron diffraction line profile analysis.[40]

Today, XRD was used in three forms containing single crystal x-ray diffraction, powder diffraction, and grazing incidence diffraction. A monochromatized x-ray beam was used in these techniques.[41] XRD analysis is an appropriate method to analyze the phase and the structural properties of single crystals and/or polycrystalline materials. Investigation of the mechanical behavior of micro-/nano scale structures of electronic devices was very important. The mechanical properties of metals were dependent on the feature size. For example, the yield strength of Au was increased by 80 times, when its dimensions were decreased to smaller than 1 μm. This phenomenon can be due to the dislocation starvation effect. According to this theory, mobile dislocations can annihilate without any interferences to other defects with gliding along their slip planes to the free surfaces. Therefore, the mobile dislocation density in the nanostructures was decreased during mechanical formation. Consequently, a decrease in the size of nanostructures leads to a decrease in the number of dislocation sources, and therefore, the operation strength of nanostructures was increased.[42]

A non-destructive synchrotron Laue x-ray microdiffraction (μSLXRD) method with polychromatic white beam was used to study *ex situ* characterization of the defect density before and after the compression tests. In this method, the unit cell size of crystal structures can be obtained using the wavelength of each reflection. In addition, the lattice strain and crystalline orientations were determined using Laue patterns. An x-ray synchrotron was used as a source in Laue x-ray diffraction. This method was used to investigate *in situ* phase transformation like martensitic

transformations, and structural and mechanical properties of microelectronic devices.[41] This technique can detect either statistically stored dislocations (SSD) and/or geometric necessary dislocations (GND).[42] The total Burgers vector in SSDs is zero, which cause a symmetrical shape of diffraction peaks and broadening of the diffraction peak. While, GNDs are unpaired dislocations, for which their Burgers vector does not equal zero and contains a local lattice curvature. Therefore, there is a change in the orientation of the lattice planes and the diffraction vectors, which lead to a streaking of diffraction peaks. The type of GNDs can be detected using the examination of the streaking direction of the Laue spots.[1] This method was applied to study the crystalline properties of small-size materials (microscale), pure materials, localized volume of materials, and microstructure and stress in electronic devices. By analyzing the Lauegram, the x-ray peaks of individual grains can be indexed. In addition, this method can measure the grain rotation, stress/strain tensors, plastic deformation, and the density of GND dislocations. The high energy of the synchrotron beam (5–24 keV) can characterize the grain size with 100 nm, and can penetrate up to 1 mm into Si,[43] and as a result of that, the residual stress in the Si can be estimated using this technique.[2]

This technique has been used to determine the piezoelectric coefficients of thin films. It can record very small displacement of the surface with high strain sensitivity. The switching behavior, electromechanical properties, and polarization fatigue of PZT thin films can be measured using this technique.[44] In addition, this technique was used to study the thermal behavior of martensitic transformation in zirconia (with submicron resolution).[45]

The focused x-ray probe on samples was micro/-nano-sized. Therefore, the crystalline phases in small crystals, phase transformation, orientation mapping of crystals, elastic strain–stress, and the crystalline defects can be identified using this technique. Due to the high flux of the synchrotron x-ray beam, a Laue pattern (LP) of a bulk crystal was taken during 1 s.[46] Micro-Laue diffraction presents map strains in micrometer-thick films, which can provide a high resolution to investigate the strains within grains. Investigation of the intragrain strains requires a nano-beam. Coherent x-ray diffraction (CXD) is a very powerful technique to obtain *3D* map strains with high resolution (10 nm order resolution).[47]

In the perfect single crystal, the Laue pattern would most closely resemble the reciprocal of the infinite single perfect crystal planes. Nevertheless, in the ploy-crystalline materials that deviated from an ideal single crystal, the x-ray diffraction peak broadening was observed caused by both crystallite size and lattice strain due to higher angle of boundaries or grain sub-structures.[48] In this case, the lattice is strained, as what is initially one crystal, so it "breaks" into like two crystals thus forming substructure or what could be seen like "grain boundary". Therefore, the peak broadening must be considered to examine the structural properties of materials. The small crystallites and defects (such as dislocations) in materials lead to broadening their diffraction peaks.[39] Accordingly, some of XRD parameters such as the peak width, intensity of the peaks, and XRD peak shift were originated by the crystallite size and the lattice strain, Fig. 2. The crystallite size and lattice strain were related to the Bragg's angles as $1/\cos\theta$ and $\tan\theta$, respectively.[49] This correlation was first illustrated by Budiman et al. in their polycrystalline samples that had gone through electromigration, which is an electron wind force large enough that could push atoms and cause migration of atoms (a common material degradation mechanism in microelectronics chip-level interconnects.).

Budiman et al. have observed the plasticity in the Cu grains through the line caused by the EM test progression. The plasticity of Cu grains can be existing in the form of diffraction spot broadening (streaking) and in the form of diffraction spot splitting (into two or even more different spots), which related to the crystal bending of the Cu grains in the line and the formation of low angle boundaries or subgrain structures, respectively. The bending of the Cu crystal and the degree of splitting can be measured using the amount of broadening and the angle of misorientation between subgrains, respectively.[50] Figure 2b shows the effect of dislocation on the broadening utilizing electromigration (EM). A split diffraction spot was formed by increasing applied current and time of EM, which showed the formation of low-angle grain boundaries. The grains can split into two spots when the EM test progresses. The geometrically necessary dislocation density (GND) was calculated using the Cahn-Nye formula, $\rho = 1/Rb$, where R and b are the radius of the curvature of the grain and the Burgers vector, respectively.[51]

Crystallite size has coherent diffraction domains in x-ray diffraction. In addition, the crystallite size of the particles differed as to the particle size due to the presence of grain boundaries and/or ploy-crystalline aggregates.[52] The generation of strain in the crystalline lattices may be caused by several factors such as crystal imperfections, lattice dislocations, grain boundary triple junctions, contract or sinter stresses, stacking faults, coherency stresses, etc.[53]

Based on the results of the XRD pattern, several methods have been used to estimate the crystallite size and lattice strain of materials. In the present

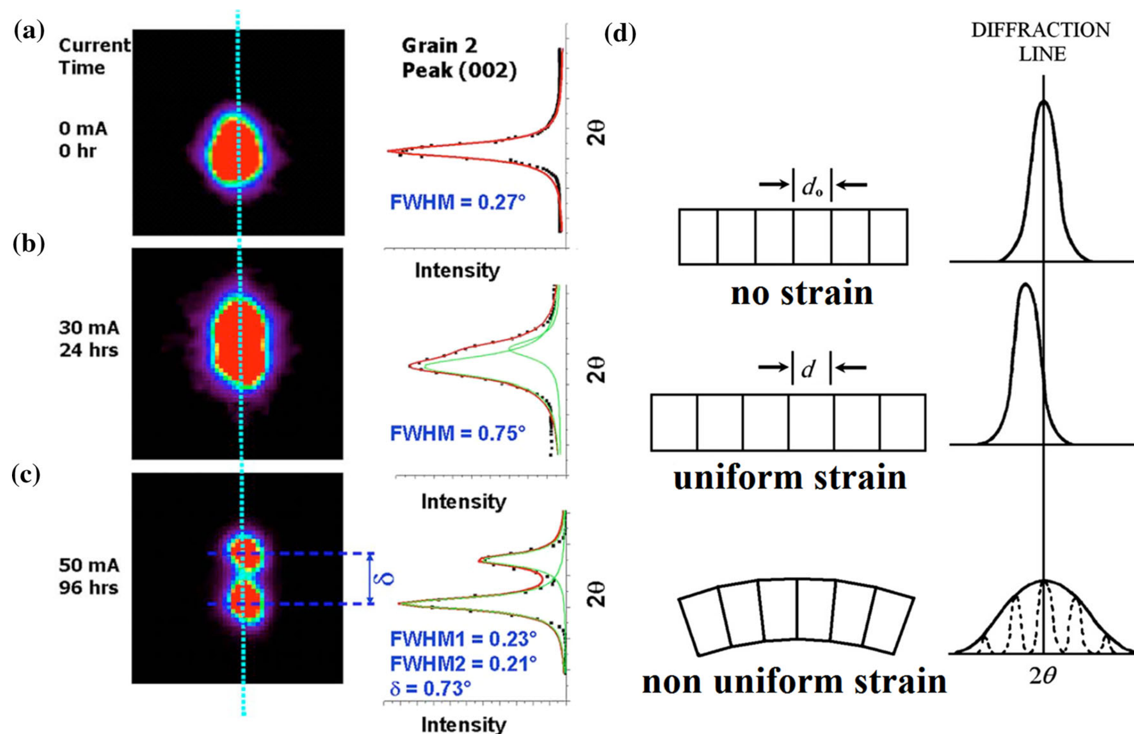

Fig. 2. The effect of dislocation on the (a) Laue peak broadening, (b) peak splitting (i.e., grain bending or GND, followed by grain substructure formation which is like a grain boundary as the crystal almost breaks into two crystals), (c) as EM progresses, "Reprinted from [A. Budiman, W. Nix, N. Tamura, B. Valek, K. Gadre, J. Maiz, R. Spolenak, and J. Patel, Applied Physics Letters 88, 233515 (2006)], with the permission of AIP publishing.", and (d) the effect of uniform and nonuniform strain on the peak broadening.

research, we apply three methods including Scherrer's method, Williamson–Hall (W–H) method, and size–strain plot (SSP) method. In the Scherrer's method, the crystallite size was estimated using the breadth of the diffraction peak. The Bragg breadth contribution originated from crystallite size is in inverse relation to the crystallite size. However, it should be noted that the influence of inhomogeneous strain and instrumental effect on the peak broadening has not been considered in the Scherrer's method. Therefore, the Debye–Scherrer's (D–S) method offers only a lower bound on the crystallite size.[48] Among different methods to analyze and/or estimate the crystallite size and lattice strain contributions to the line broadening [Warren–Averbach (W–A) analysis, W–H analysis, Fourier technique, and Rietveld refinement], W–H analysis is a simple method to determine the size- and strain induced peak broadening by considering the variation of peak broadening versus 2θ. In the higher angle reflections, at least two reflections along the same crystallographic direction were needed to examine the structural properties of materials using W–A analysis, and the convolution of the size and strain broadening occurred in the Fourier technique. Accordingly, these techniques are very complicated.[54] Strain broadening was dependent on planar defects, stacking faults, and dislocations. Among these, dislocation plays a special and unique role. Therefore, investigation of the effect of dislocation on the strain broadening was very important. In the W–H method, strain anisotropy is described by the dislocation model of the mean square strain. The strain broadening was dependent on the orientations of the line and the Burgers vectors of the dislocations.[39]

In this paper, undoped and Se-doped SnS thin films were synthesized using an electrochemical method. Then, the effect of Se-dopant concentration was investigated on the structural properties of SnS thin films. The current research presents a comprehensive study on crystallite size and lattice strain of undoped and Se-doped SnS thin films. The estimation of structural parameters such as crystallite size, lattice strain, and lattice stress was done using various methods. The crystallite size is evaluated using Debye–Scherrer's method, W–H method, and the size strain plot (SSP) method. In addition, the lattice strain was estimated using three Williamson-Hall models, namely, a uniform deformation model (UDM), a uniform stress deformation model (USDM), a uniform deformation energy density model (UDEDM), and the size strain plot method (SSP). To the best of our knowledge, the study on the structural properties of Se-doped SnS thin films using various methods including D-S,

UDM, UDSM, UDEDM, and SSP has not been yet reported.

EXPERIMENTAL

Materials and Processing

Nanostructured undoped and Se-doped SnS thin films were prepared using a three-electrode electrochemical cell. The cathode was fluorine-doped tin oxide (FTO) coated glass substrate with a dimension of 2 cm × 1 cm. The effective area of substrates was 1 cm × 1 cm with 8 Ω/cm sheet resistance. A platinum electrode was used as the anode. The reference electrode was a saturated calomel electrode (SCE). An aqueous electrolyte containing 2 mM $SnCl_2$ and 16 mM $Na_2S_2O_3$ was prepared in a beaker. Se-doped SnS thin films with different concentrations of Se-dopant were produced by adding different amounts of SeO_2 (4 mM) solution to the electrolyte. By drop wise adding the diluted H_2SO_4, the pH of solution was reduced from 3.8 to 2.1. The undoped SnS was named as the Se1 sample. In addition, the Se2, Se3, Se4, Se5, and Se6 samples were prepared by adding 1.0 mL, 1.5 mL, 2 mL, 8 mL, and 12.5 mL of SeO-$_2$ solution, respectively, into the electrolyte.

The glass substrates and the platinum electrode were washed with an ultrasonic cleaner, and then they were rinsed with ethanol/acetone and distilled water. The temperature of the bath remained at 60°C. The solution was stirred consistently at 750 rpm. The time of electrodeposition process was 30 min for all samples. A computer-controlled electrochemical analyzer (potentiostat, Autolab, A3ut71167, Netherlands) was used to control the deposition potential at − 1 V for all samples. After the deposition process, the substrates were taken out of the bath. Then the samples were washed with distilled water and finally dried with an air jet. The deposited films showed strong adherence to the substrate. According to the following reactions, SnS was formed on the cathode electrode (FTO substrate):

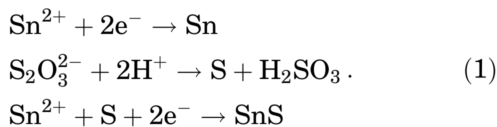

$$\begin{aligned} & Sn^{2+} + 2e^- \rightarrow Sn \\ & S_2O_3^{2-} + 2H^+ \rightarrow S + H_2SO_3 \, . \\ & Sn^{2+} + S + 2e^- \rightarrow SnS \end{aligned} \tag{1}$$

As it is observed in the above reactions, the $Na_2S_2O_3$ is unstable in acidic solution, and the sulfur can be separated very easily. Therefore, Sn^{2+} and S were reduced at the cathode (substrate) to form SnS.

In this research, our experiments are performed on six samples containing undoped SnS (Se1) and Se-doped SnS thin films with different amounts of Se-dopant. The atomic percentage of Se-dopant in the Se1, Se2, Se3, Se4, Se5, and Se6 samples were 0.00%, 0.77%, 1.30%, 2.32%, 3.92%, and 7.64%, respectively.

Characterization of the Films

A Philips X'Pert-MPD x-ray diffraction diffractometer (XRD) system with Cu-Kα radiation was employed to check the structural phases of thin films. The focus x-ray beam size on samples was 10 mm × 10 mm. In order to study the shape and size of SnS particles, A PHILIPS CM120 TEM with 100,000× magnification was used. A TE-SCAN field emission scanning electron microscope (FESEM) was used to investigate the size of samples.

RESULTS AND DISCUSSION

XRD Patterns

X-ray diffraction is an appropriate method to analyze the structural phases of materials. The XRD patterns of undoped and Se-doped SnS thin films with 2θ range of 20-60° are shown in Fig. 3. As can be seen in Fig. 3a, all peaks were well matched with orthorhombic SnS, which it found in the standard reference data (JCPDS: 039-0354, its lattice constants: a = 4.3291 Å, b = 11.1923 Å, c = 3.9838 Å with a/c = 1.086). The Se-dopant did not affect the crystalline structure of SnS. However, due to the difference in the effective ionic radii of Se^{2-} and S^{2-} ions, Se-dopant causes the change in the structural parameters such as lattice parameters, unit cell volume, and inter-planar distance of SnS lattice. In addition, no trace of Se, SnSe, SeO_2, and/or other impurities could be seen. Although, the peak located at 33.80° has arisen from the FTO substrate. It is clear that the sharpness of undoped SnS sample peaks has been increased with 2.32% Se-doping. It means that the crystalline quality of undoped SnS was increased after Se-doping, which causes an increase in the crystallite size. The improvement in the crystalline quality of SnS thin films after Se-doping, up to 2.32%, can be due to the following reasons: (1) the development in the growth process resulting from generating of new nucleation centers,[55] and (2) the creation of a small mismatch arising from introduction of Se-dopant in the space between double-layers perpendicular to the c-axis, which were bounded by weak Van der Waals' forces (see Fig. 1).[56] As the Se-dopant concentration exceeds 2.32%, Se-dopant could substitute the host S atoms, which resulted in the destruction of the periodicity of the SnS lattice. In addition, the difference between the effective ionic radius of Se^{2-} (1.98 Å) and S^{2-} (1.84 Å) leads to creating lattice mismatch and/or lattice distortion. Therefore, the crystalline quality of SnS was decreased. Consequently, it can be said that at lower concentration of Se-dopant (up to 2.32%), the incorporation of Se-dopant in the SnS lattice is interstitial and it is substitutional at higher concentrations.

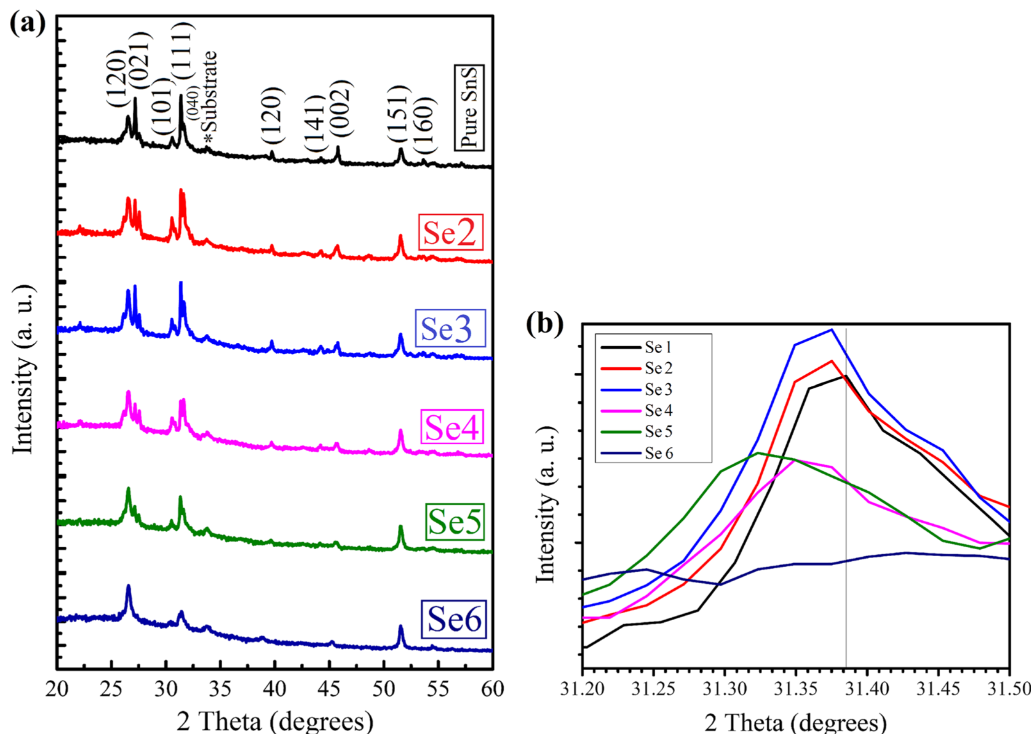

Fig. 3. (a) XRD patterns of undoped and Se-doped SnS thin films, and (b) the shift of (111) diffraction peak.

Figure 3b shows the shifting of (111) diffraction peak for undoped and Se-doped SnS thin films. It is clear that the (111) peak of undoped SnS sample is shifted toward smaller 2θ positions due to Se-doping. This occurrence could be explained using Bragg's law, as follows,

$$n\lambda = 2d_{hkl} \sin\theta_B, \quad (2)$$

where n is a positive integer and λ is the wavelength of incident x-ray (0.154056 nm), d_{hkl} is the interplanar space, and θ_B is the Bragg's angle. According to Eq. 2, the d_{hkl} and θ_B are reciprocal to each other. As Se-dopant introduces into the SnS lattice, the d_{hkl} was increased due to greater effective ionic radii of Se^{2-} than that of S^{2-} ions, which causes a decrease in the Bragg's angle. Therefore, the position of 2θ was shifted toward smaller angles, after Se-doping (see Fig. 3b). This is confirmed that the successful doping of Se-dopant into the SnS lattice.

Crystallite Size and Lattice Strain

Scherrer's Method

A combination of instrument-dependent effect and sample-dependent effect produced the breadth of the Bragg's peak. The standard materials such as silicon or aluminum were used to measure the line broadening of instrument-dependent effect. The instrumental corrected broadening (β_{hkl}) was related to the diffraction peak of SnS which was obtained using the following relation,[52,57]

$$\beta_{hkl} = \left[(\beta_{hkl})^2_{\text{measured}} - (\beta_{hkl})^2_{\text{instrumental}}\right]^{\frac{1}{2}}. \quad (3)$$

Scherrer's equation was utilized to calculate the crystallite size broadening,[57]

$$\beta_{hkl} = k\lambda / D\cos\theta_B, \quad (4)$$

where β_{hkl} is instrumental corrected broadening, k is a constant (0.94), λ is the wavelength of x-ray, D is the crystallite size (nm), and θ_B is the Bragg's angle. Figure 4 shows the plots of cos θ versus $1/\beta_{hkl}$ for undoped and Se-doped SnS thin films. According to Eq. 4, the crystallite size (D) can be obtained from the slope of this plot. The crystallite size equals $k\lambda$/(*slope*). Therefore, considering the values of k (0.94) and λ (0.154056 nm), the crystallite size was obtained using the 0.144812/(*slope*) relation. According to Fig. 4, the crystallite size of undoped SnS thin film was increased after Se-doping from 75.00 nm to 84.16 nm, and then it was decreased to 52.44 nm. Therefore, it can be said that the appropriate concentration of Se-doping (up to 2.32%—Se4

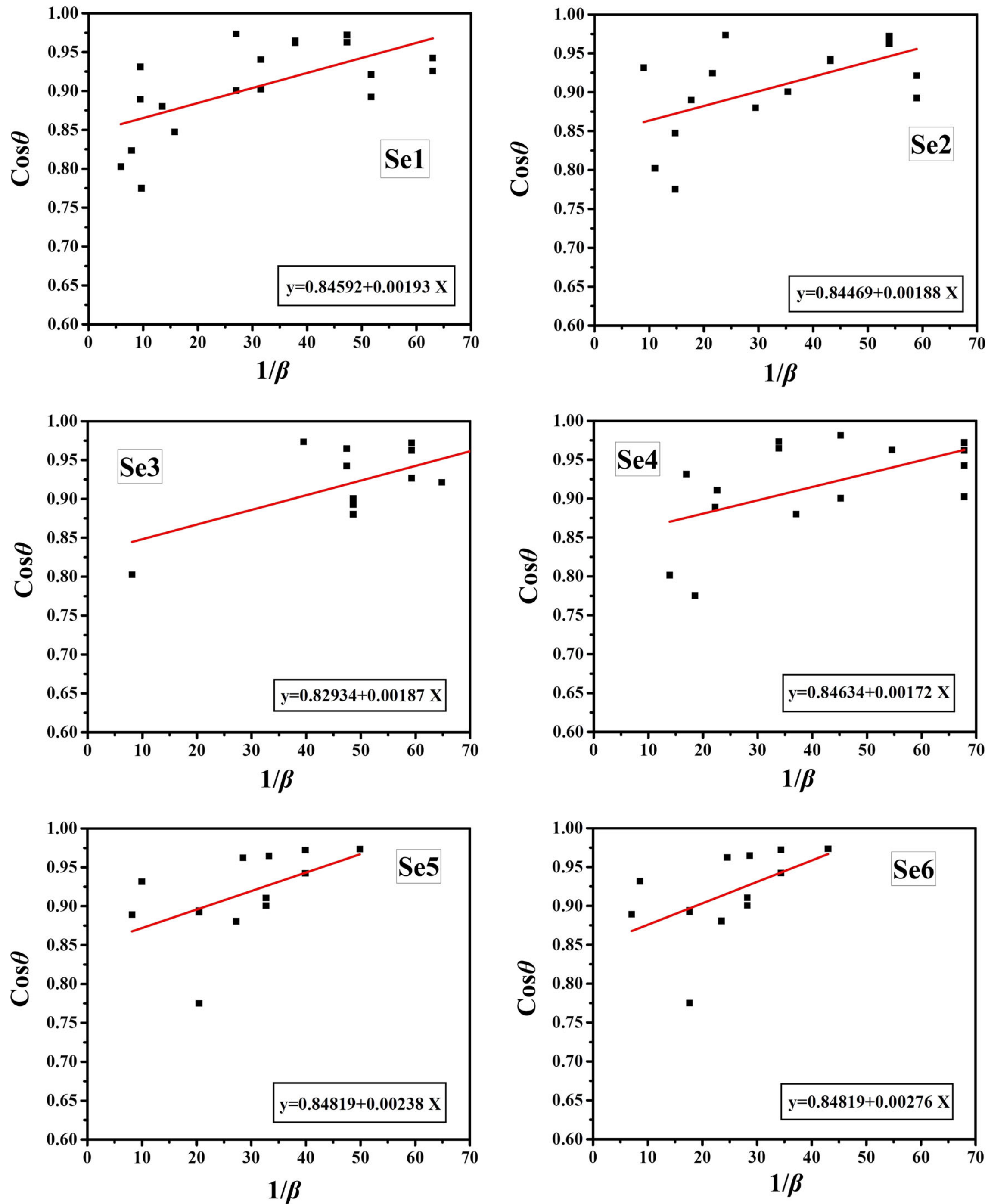

Fig. 4. Scherrer's plots of undoped and Se-doped SnS thin films.

sample) leads to an improvement in the crystalline quality of SnS thin films. It is noted that the broadening of diffraction peaks can be due to the lattice strain/size effect and non-stoichiometric sulfide defects in the SnS lattice.[58] As the Scherrer's method does not cover the crystalline imperfections and strain distribution, the Williamson-Hall and size–strain plot methods have been used.

Williamson–Hall Method

The Williamson–Hall method was based on the combination of two terms including size broadening (β_s) and strain broadening (β_ε). In this paper, we present three models of Williamson–Hall analysis containing a uniform deformation model (UDM), a uniform deformation stress model (UDSM), and a uniform deformation energy density model (UDEDM). The UDM model was based on the isotropic nature of crystals. In this model, the lattice strain is uniform in all crystallographic directions.[59] The presence of imperfections and distortions in crystals leads to create the strain broadening term. As it is mentioned above, size-broadening term can be obtained using Scherrer's formula (Eq. 4), and the strain-broadening term is given by the Wilson formula,[54]

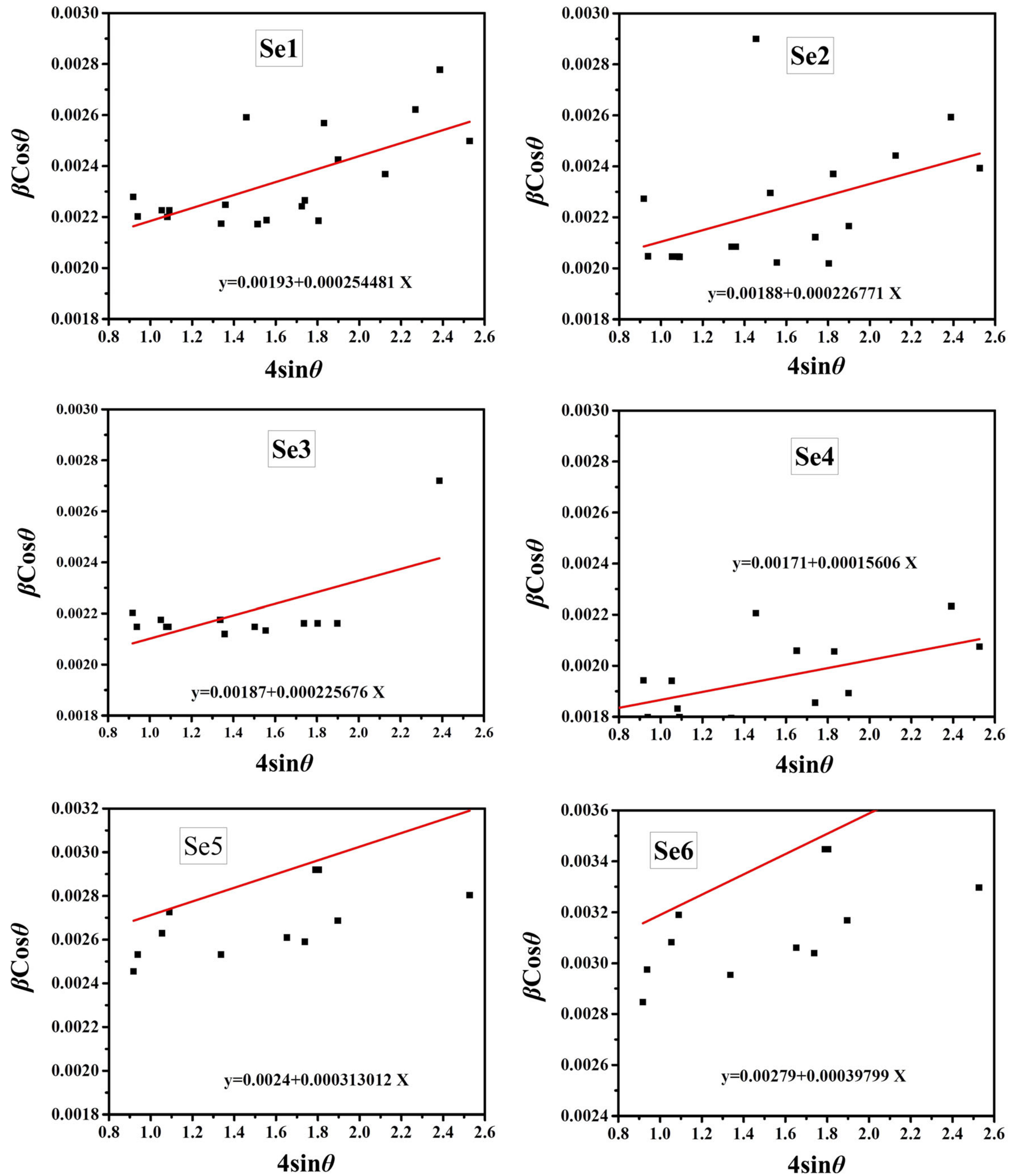

Fig. 5. The plots of W–H method assuming UDM model for undoped and Se-doped SnS thin films.

$$\beta_\varepsilon = C\varepsilon \tan\theta, \tag{5}$$

where ε is the tensile or compressive strain, and C is a constant which was taken 4. It is assumed that the crystallite size and the lattice strain are independent of each other and both have the Cauchy-like profile. Then, by combining the two abovementioned terms, the Williamson–Hall equation was deduced in Eq. 8.[54,60,61]

$$\beta_{hkl} = \beta_S + \beta_\varepsilon \tag{6}$$

$$\beta_{hkl} = (k\lambda)/(D\cos\theta) + 4\varepsilon\tan\theta \tag{7}$$

$$\cos\theta \times Eq.y \Rightarrow \beta_{hkl}\cos\theta = k\lambda/D + 4\varepsilon\sin\theta \tag{8}$$

Equation 8 shows the uniform deformation model (UDM) of the Williamson-Hall method. As it is obvious in Eq. 8, the estimation of lattice strain and crystallite size was easy by drawing the graph of β_{hkl} cos θ against 4sin θ. The D and ε were obtained using the y-intercept at $x = 0$ and the slope of this plot, respectively. Figure 5 illustrates the UDM plots of undoped and Se-doped SnS thin films. As it is clear, the crystallite size of SnS films increased from 75 nm to 84 nm, and then decreased to 52 nm, due to Se-doping. It means that the crystalline quality of undoped SnS was initially increased and then decreased after Se-doping. The reason is the fact that the lattice strain (ε) has an inverse relation to the D, which decreased from 2.54×10^{-4} (Se1) to 1.56×10^{-4} (Se4) and then increased to 3.97×10^{-4} for the Se6 sample. The creation of new nucleation centers due to Se-doping (up to 2.32%) can lead to improvement in crystalline quality. Therefore, the lattice strain was decreased. However, further Se-doping in the SnS lattice leads to a decrease in crystalline quality and an increase in lattice strain due to the following reasons: (1) the difference between the effective ionic radii of Se^{2-} and S^{2-} can generate lattice distortion, (2) saturation of nucleation centers and/or lattice distortion, and (3) existence of Se^{2-} ions in the electrolyte can delay the reaction between Sn^{2+} and S^{2-} ions. In addition, based on the Quin and Szpunar model, the grain boundary excess volume related to vacancies and vacancy clusters can produce the strain in the lattice.[62]

Based on the anisotropic nature of Young's modulus (E_{hkl} or Y_{hkl}),[63] two modified W–H models named UDSM and UDEDM have been used. The D, ε, lattice strain (σ), and energy density (u) could be estimated using UDSM and UDEDM models. According to Hooke's law ($\sigma = Y_{hkl} \times \varepsilon$), the lattice stress and lattice strain are linked together with the elastic modulus (Young's modulus) coefficient. It should be noted that the Hooke's law only validates in the elastic zone. Therefore, assuming very small strains in the undoped and Se-doped SnS lattices, the UDSM and UDEDM models can be used. By applying Hooke's law in the W–H equation (Eq. 8), the lattice strain is replaced by ($\varepsilon = \sigma/Y_{\mathrm{hkl}}$). Therefore, the UDSM equation was obtained by the following formula,

$$\beta_{hkl}\cos\theta = \frac{k\lambda}{D} + 4\left(\frac{\sigma\sin\theta}{E_{hkl}}\right). \tag{9}$$

The crystallite size (D) and lattice stress (σ) can be obtained by the UDSM model. The UDSM graphs were achieved by drawing β_{hkl} cosθ and 4sin θ/E_{hkl} along the y-axis and x-axis, respectively. The slope of this graph showed the lattice stress (σ) and the D was estimated by y-intercept ($D = (k\lambda)/(y$-intercept)), similar to the UDM model. Therefore, the lattice strain of undoped and Se-doped SnS thin films was estimated using the $\varepsilon = \sigma/Y_{hkl}$ relation. The reciprocal of Young's modulus in the direction of the unit vector l_i in the orthorhombic structures is given by the following formula,[64]

$$\frac{1}{Y_{hkl}} = l_1^4 s_{11} + 2l_1^2 l_2^2 s_{12} + 2l_1^2 l_3^2 s_{13} + l_2^4 s_{22} + 2l_2^2 l_3^2 s_{23} + l_3^4 s_{33} + l_2^2 l_3^2 s_{44} + l_1^2 l_3^2 s_{55} + l_1^2 l_2^2 s_{66}. \tag{10}$$

The following relations present the unit vectors (l_{i}) for a particular (hkl) plane,

$$l_1 = \frac{h}{\sqrt{h^2+k^2+l^2}}, \quad l_2 = \frac{k}{\sqrt{h^2+k^2+l^2}}, \quad l_3 = \frac{l}{\sqrt{h^2+k^2+l^2}} \tag{11}$$

where s_{11}, s_{12}, s_{13}, s_{22}, s_{23}, s_{33}, s_{44}, s_{55}, and s_{66} are the elastic compliance of SnS with values of 11.92 $(\mathrm{TPa})^{-1}$, − 2.93 $(\mathrm{TPa})^{-1}$, − 4.32 $(\mathrm{TPa})^{-1}$, 10.07 $(\mathrm{TPa})^{-1}$, − 8.2 $(\mathrm{TPa})^{-1}$, 19.08 $(\mathrm{TPa})^{-1}$, 19.46 $(\mathrm{TPa})^{-1}$, 35.8 $(\mathrm{TPa})^{-1}$, and 35.27 $(\mathrm{TPa})^{-1}$, respectively. Figure 6 exhibits the UDSM graphs of undoped and Se-doped SnS thin films. The Young's modulus of SnS was taken as 62.19 GPa.[65] As it is clear in Fig. 6, the obtained D and ε values from UDSM model are in agreement with those of the UDM model.

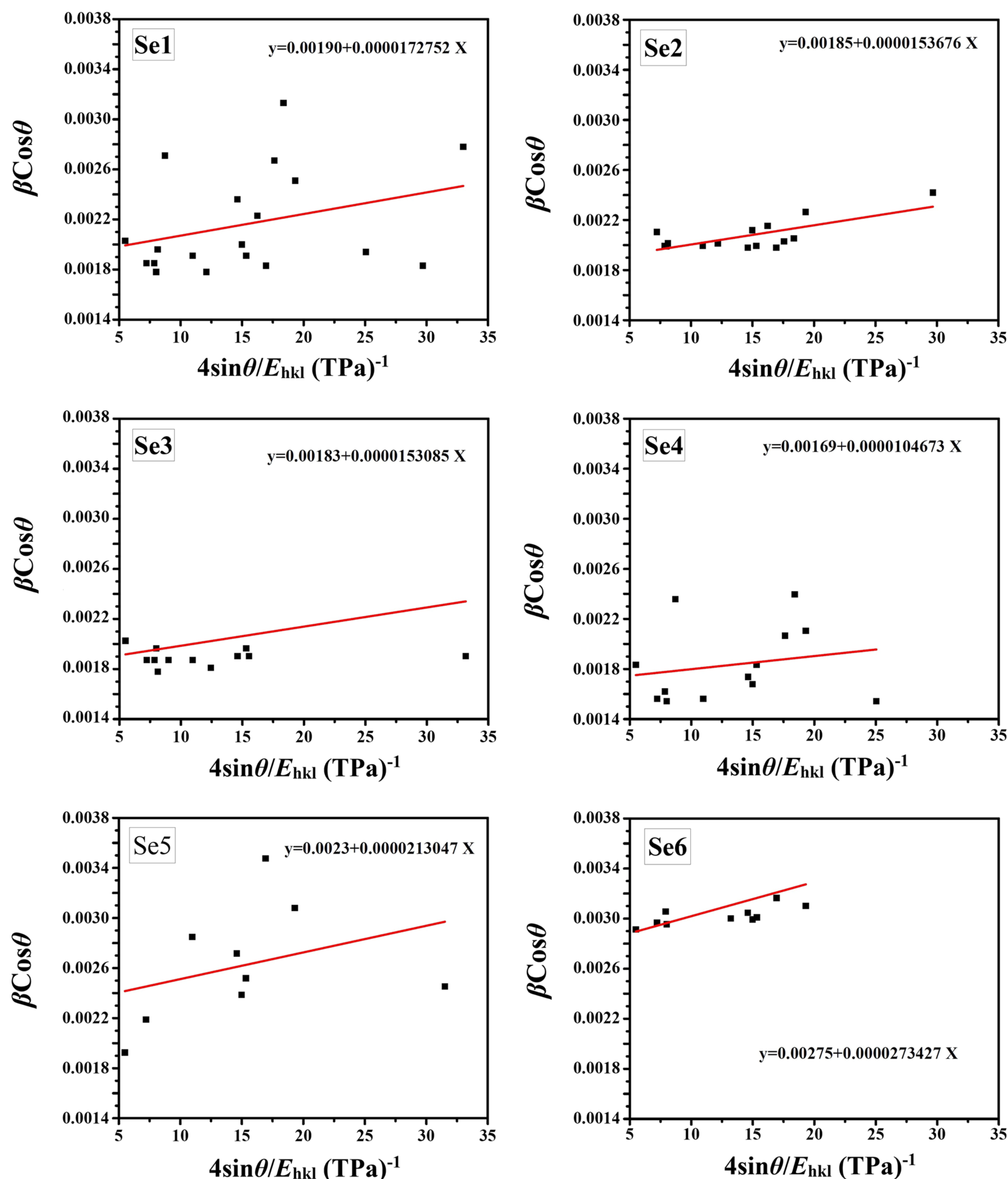

Fig. 6. The modified form of the W–H method supposing the UDSM model for undoped and Se-doped SnS samples.

Uniform deformation energy density model (UDEDM) is an appropriate model to estimate D, ε, σ, and u (energy per unit volume). According to Hooke's law, the relation between u (energy per unit volume) and ε is $u = \varepsilon^2 \times E_{hkl}/2$. Therefore, the UDEDM relation was obtained by modifying Eq. 9, as follows,[66]

$$\beta_{hkl}\cos\theta = k\lambda/D + \left(\frac{4\sin\theta}{(Y_{hkl}/2)^{1/2}}\right) \times u^{\frac{1}{2}}. \quad (12)$$

The plot of β_{hkl} cos θ versus 4sin $\theta/(Y_{hkl}/2)^{1/2}$ has been drawn to estimate the D and u. The modified W–H plots assuming the UDEDM model for

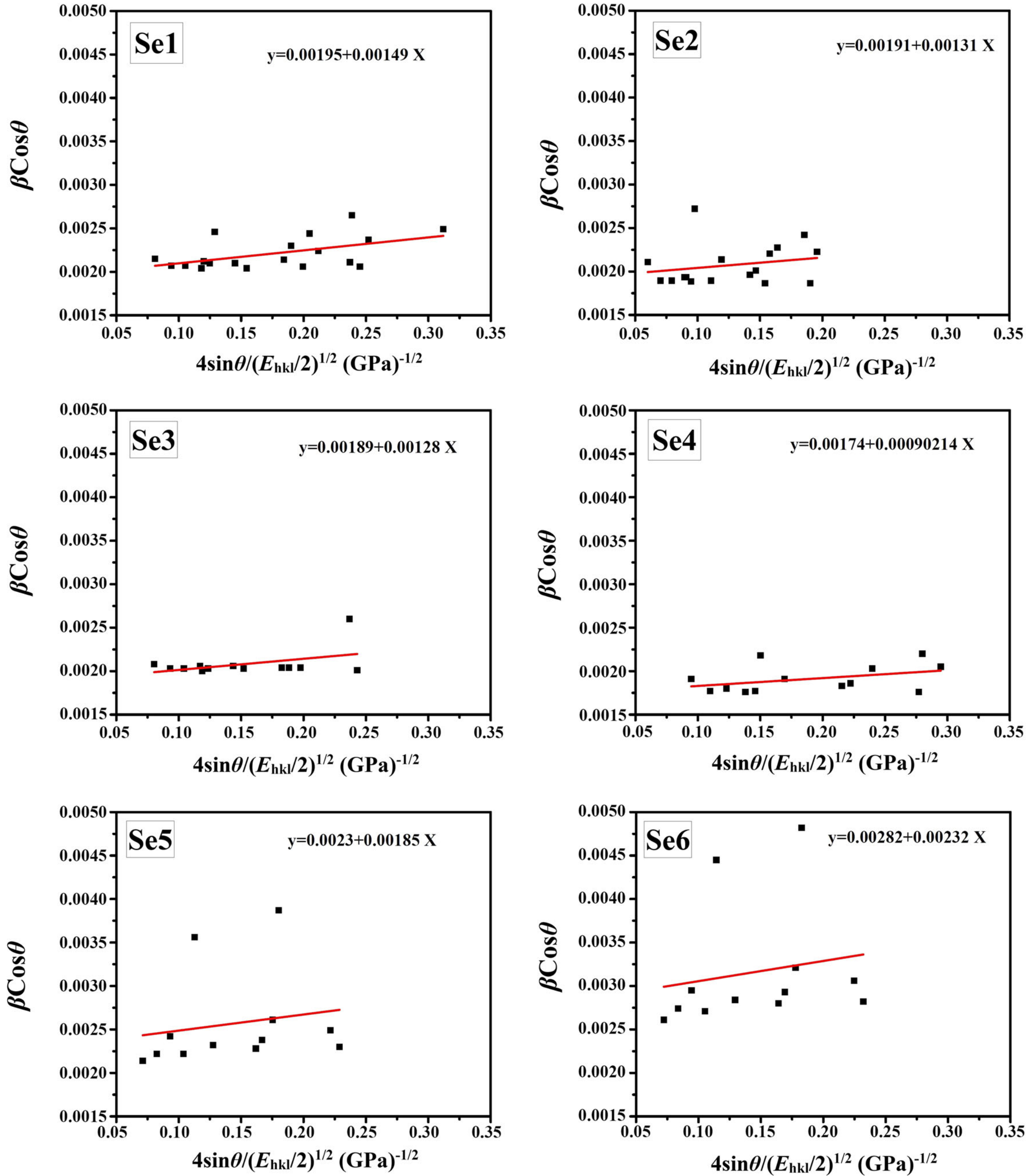

Fig. 7. The modified form of W–H analysis supposing UDEDM model for undoped and Se-doped SnS thin films.

undoped and Se-doped SnS thin films are shown in Fig. 7. The crystallite size and the energy density were calculated using the y-intercept and the square of slope, respectively. As a result, the σ and ε can be obtained assuming the Hooke's law relations,

$$\begin{aligned} \varepsilon &= (2u/Y_{hkl})^{1/2} \\ \sigma &= (2uY_{hkl})^{1/2} \end{aligned}. \tag{13}$$

The results showed that by introducing the Se-dopant into the SnS lattice, the energy density of

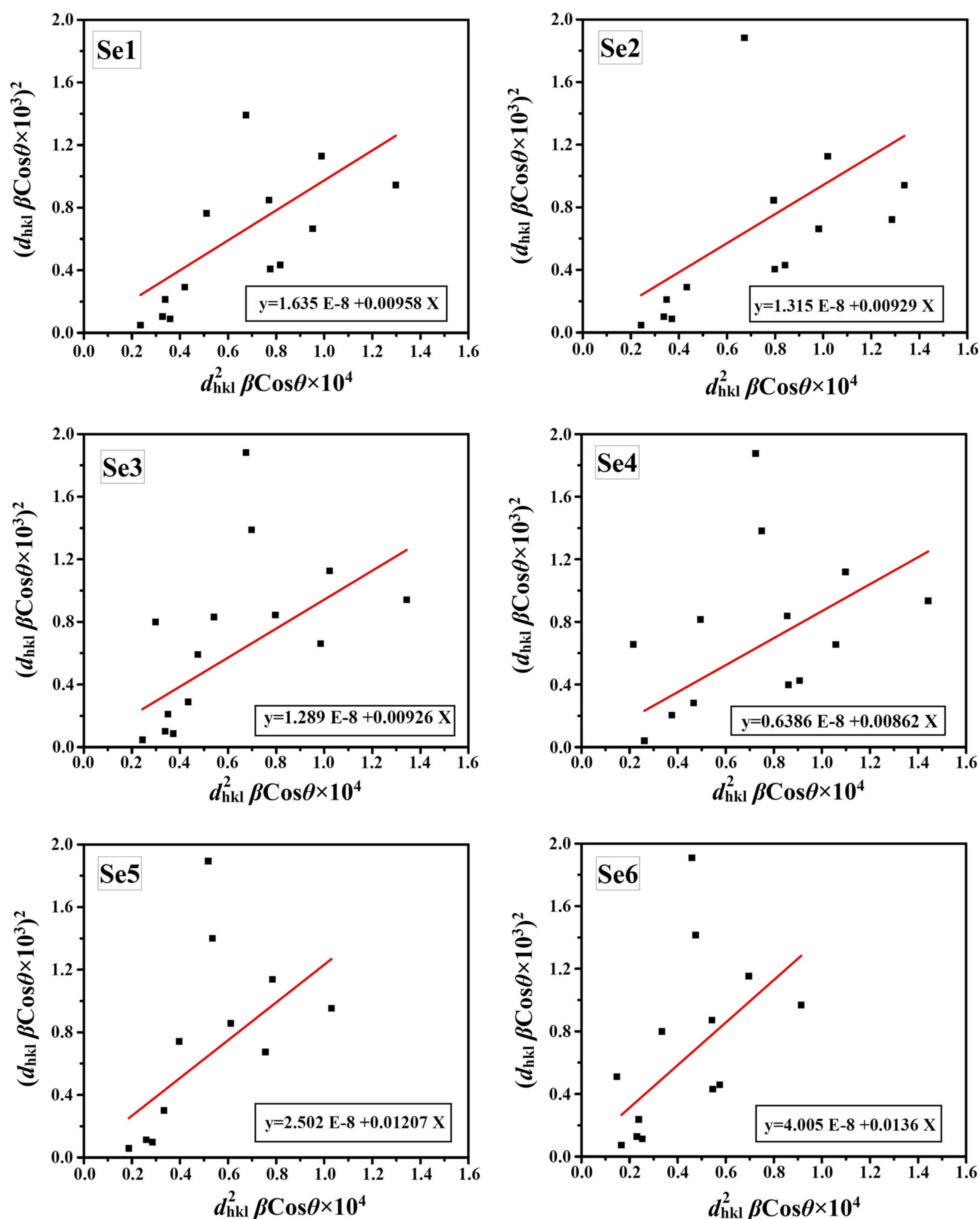

Fig. 8. Size–strain plots (SSP) for undoped and Se-doped SnS thin films.

undoped SnS was decreased to 0.81 kJ m^{-3} (Se4) and then increased to 5.38 kJ m^{-3} (Se6). The initial reduction in the energy density of undoped SnS after Se-doping can be due to the improvement in the crystalline quality which caused a decrease in the lattice strain (ε) and lattice stress

Table I. Geometric parameters of undoped and Se-doped SnS thin films

Sample	Scherrermethod	Williamson–Hall method									Size–strain plot method			
		UDM		UDSM			UDEDM							
	D (nm)	**D (nm)**	$\varepsilon \times 10^{-4}$	**D (nm)**	$\varepsilon \times 10^{-4}$	σ (MPa)	**D (nm)**	$\varepsilon \times 10^{-4}$	σ (MPa)	**U** (Kjm^{-3})	**D (nm)**	$\varepsilon \times 10^{-4}$	σ (MPa)	**U** (Kjm^{-3})
Se1	75.00	75.00	2.54	76.18	2.49	17.27	74.23	2.53	17.51	2.22	78.28	2.56	17.67	2.26
Se2	77.00	77.00	2.26	78.24	2.22	15.36	75.79	2.23	15.40	1.72	80.73	2.29	15.82	1.81
Se3	77.41	77.41	2.25	79.10	2.21	15.30	76.59	2.18	15.04	1.64	80.99	2.27	15.69	1.78
Se4	84.16	84.65	1.56	85.65	1.51	10.46	83.19	1.53	10.60	0.81	87.00	1.60	11.04	0.88
Se5	60.82	60.31	3.13	62.93	3.08	21.30	62.93	3.15	21.75	3.42	62.13	3.16	21.85	3.45
Se6	52.44	51.88	3.97	52.64	3.95	27.34	51.33	3.95	27.27	5.38	55.14	4.00	27.66	5.53

(σ). In addition, as the Se-doping was more than 2.32% in the SnS lattice, the crystalline quality declined which resulted in an increase in the energy density of the Se-doped SnS lattice. It can be concluded that the results of UDM, UDSM, and UDEDM models are well matched to each other.

Size–Strain Plot Method (SSP)

Nelson–Riley is a good method to estimate the size–strain parameters. This technique was considered for the isotropic nature of the crystal structure.[67] This method provides an accurate estimation of size–strain parameters, which gives less weight to data from reflections at high angles, where the accuracy is typically lower.[68] In this method, the crystallite size profile was defined by a "Lorentzian" function and the strain profile by a "Gaussian" function. The following formula shows the SSP method relation,[69,70]

$$(d_{hkl}\beta_{hkl}\cos\theta)^2 = \frac{K}{D}(d_{hkl}^2\beta_{hkl}\cos\theta) + (\frac{\varepsilon}{2})^2, \qquad (14)$$

where K is a shape-dependent constant that is considered three-fourths for spherical particles.[70] In order to estimate the crystallite size and the lattice strain using the SSP method, the (d_{hkl} β_{hkl} cosθ)^2 was plotted against (d_{hkl}^2 β_{hkl} cosθ) for all the main orientation peaks of undoped and Se-doped SnS thin films. Figure 8 depicts the SSP plots for all samples. As it is shown, the crystallite size and the lattice strain can be acquired from the slope and y-intercept, respectively. Therefore, the crystallite size was 0.75/(*slope*) and the lattice strain was 2 × (y-intercept)$^{1/2}$. The obtained results from the Scherrer's method, UDM, USDM, UDEDM, and SSP methods are summarized in Table I. In addition, the calculated crystallite size, lattice strain, lattice stress, and energy density for undoped and Se-doped SnS samples using Scherrer's, UDM, USDM, UDEDM, and SSP methods are compared in Fig. 9.

As can be seen from Table I and Fig. 9, the results of Scherrer's, UDM, UDSM, UDEDM, and SSP methods are in good agreement to each other. Based on Scherrer's method, the broadening of diffraction peaks was only caused by reducing grain size. Therefore, a small deviation in the crystallite size was observed, compared to the other methods.[60] Furthermore, since the strain term was not considered in the Scherrer's method, the values of obtained crystallite size using this method were higher than that of W–H methods.[71] Accordingly, the crystallite size and/or the crystalline quality of undoped SnS was initially increased and then decreased, after Se-doping.

Fig. 9. Comparison between the results of Scherrer's, UDM, UDSM, UDEDM, and SSP methods for undoped and Se-doped SnS thin films, (a) crystallite size, (b) lattice strain, (c) lattice stress, and (d) energy density.

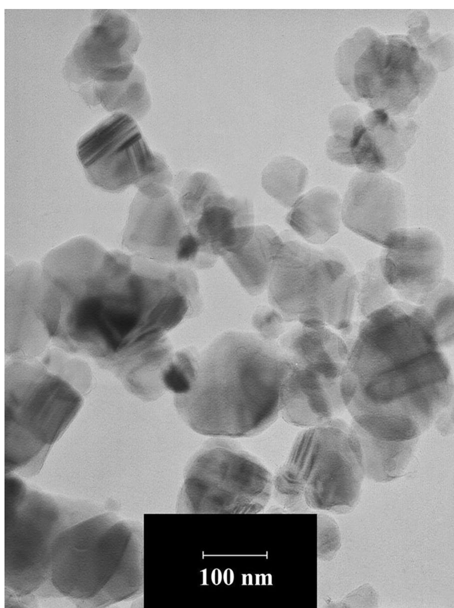

Fig. 10. TEM image of undoped SnS thin film (Se1).

Therefore, the ε, σ, and energy density (u) of undoped SnS were decreased first and then increased.

TEM Method

In order to discover the reality of obtained data from XRD analysis, TEM analysis was applied. TEM is a good study to examine the size and the shape of deposited SnS. The TEM image for undoped SnS thin film is shown in Fig. 10. It is clear in the TEM image that the average particle size is in good agreement with the average crystallite size estimated from Scherrer's, W–H and SSP methods.

Morphological Investigation

FESEM images were taken to investigate the size of deposited samples. Figure 11 showed that the dimensions of samples were micro/nano size.

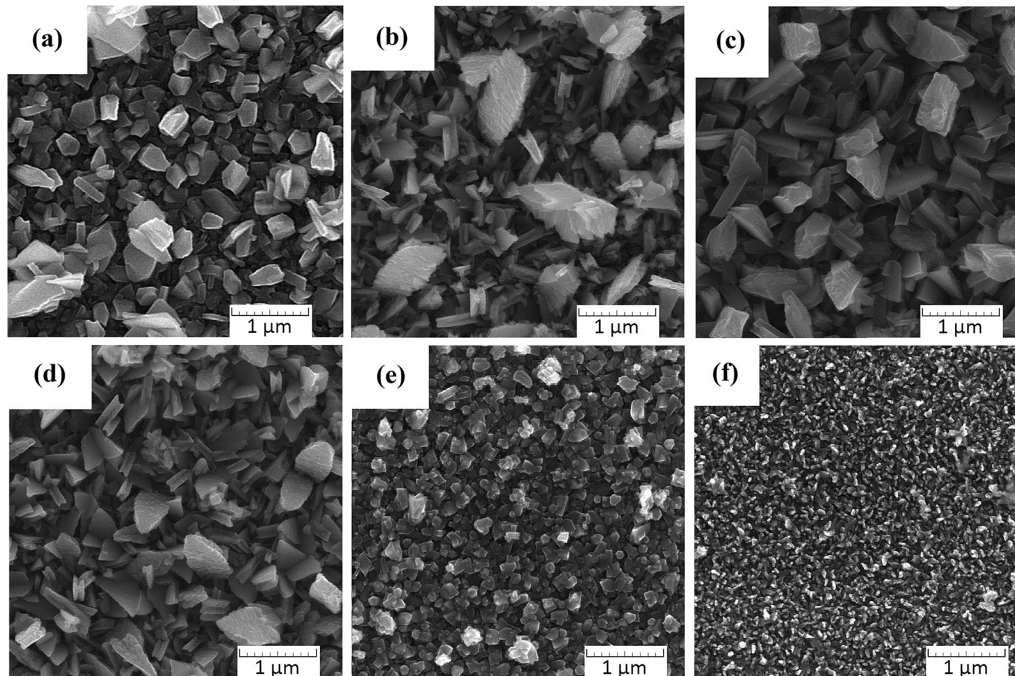

Fig. 11. FESEM images of (a) undoped SnS (Se1), (b) Se2, (c) Se3, (d) Se4, (e) Se 5, and (f) Se6 samples.

CONCLUSION

In this paper, the effect of various Se-dopant concentrations on the structural properties of SnS thin films has been investigated. Undoped SnS and Se-doped SnS thin films have been deposited on the FTO substrates using the electrodeposition method. XRD patterns confirmed that all synthesized thin films were orthorhombic. The Debye–Scherrer's technique was used to estimate the crystallite size of undoped and Se-doped SnS thin films. In addition, the modified form of the W–H method assuming a uniform deformation model (UDM), a uniform deformation stress model (USDM), a uniform deformation energy density model (UDEDM), and the size–strain plot method (SSP) have been used to calculate the crystallite size and the lattice strain of synthesized thin films. The results obtained by these methods showed that with increasing the Se-dopant concentration (up to 2.32%) in the SnS lattice, the crystallite size was increased, and the lattice strain was decreased. However, further Se-doping into the SnS lattice leads to more lattice distortion in the crystal lattice due to the variation in the effective ionic radii of Se^{2-} and S^{2-} ions, which caused a decrease in the crystalline quality and/or crystallite size. In addition, the results showed that there was a good agreement in the particle size obtained from W–H methods and the SSP method with TEM images.

REFERENCES

1. T.W. Cornelius and O. Thomas, *Prog. Mater Sci.* 94, 384 (2018).
2. S.K. Tippabhotla, I. Radchenko, K.N. Rengarajan, G. Illya, V. Handara, M. Kunz, N. Tamura, and A.S. Budiman, *Procedia Eng.* 139, 123 (2016).
3. A.S. Budiman, H.A.S. Shin, B.J. Kim, S.H. Hwang, H.Y. Son, M.S. Suh, Q.H. Chung, K.Y. Byun, N. Tamura, M. Kunz, and Y.C. Joo, *Microelectron. Reliab.* 52, 530 (2012).
4. D. Ferri, M.A. Newton, M. Di Michiel, S. Yoon, G.L. Chiarello, V. Marchionni, S.K. Matam, M.H. Aguirre, A. Weidenkaff, and F. Wen, *Phys. Chem. Chem. Phys.* 15, 8629 (2013).
5. H. Kafashan, *Ceram. Int.* 45, 334 (2019).
6. S. Polivtseva, A. Katerski, E. Kärber, I. Oja Acik, A. Mere, V. Mikli, and M. Krunks, *Thin Solid Films* 633, 179 (2017).
7. J.-Y. Kang, S.-M. Kwon, S.H. Yang, J.-H. Cha, J.A. Bae, and C.-W. Jeon, *J. Alloys Compd.* 711, 294 (2017).
8. H. Kafashan, F. Jamali-Sheini, R. Ebrahimi-Kahrizsangi, and R. Yousefi, *Int. J. Miner. Metall. Mater.* 23, 348 (2016).
9. H. Kafashan, F. Jamali-Sheini, M. Azizieh, Z. Balak, M. Cheraghizade, and H. Nasiri Vatan, *J. Alloys Compd.* 694, 1338 (2017).
10. H. Kafashan, F. Jamali-Sheini, R. Ebrahimi-Kahrizsangi, and R. Yousefi, *J. Alloys Compd.* 681, 595 (2016).
11. H. Kafashan, R. Ebrahimi-Kahrizsangi, F. Jamali-Sheini, and R. Yousefi, *Phys. Status Solidi. A* 213, 1302 (2016).
12. S. Banu, S.J. Ahn, Y.J. Eo, J. Gwak, and A. Cho, *Sol. Energy* 145, 33 (2017).
13. J. Kois, S. Bereznev, J. Maricheva, and N. Revathi, *Mater. Sci. Semicond. Process.* 58, 76 (2017).
14. B.H. Baby, V.M. Vaisakh, and D. Bharathi Mohan, *Mater. Today Proc.* 3, 2077 (2016).
15. P. Nwofe, K.R. Reddy, J. Tan, I. Forbes, and R. Miles, *Phys. Procedia* 25, 150 (2012).

16. A. Basak, A. Mondal, and U.P. Singh, *Mater. Sci. Semicond. Process.* 56, 381 (2016).
17. Y. Kawano, J. Chantana, and T. Minemoto, *Curr. Appl. Phys.* 15, 897 (2015).
18. S. Gedi, V.R.M. Reddy, J.-Y. Kang, and C.-W. Jeon, *Appl. Surf. Sci.* 402, 463 (2017).
19. F. Alam and V. Dutta, *Appl. Surf. Sci.* 358, 491 (2015).
20. G.G. Ninan, C.S. Kartha, and K.P. Vijayakumar, *J. Anal. Appl. Pyrol.* 120, 121 (2016).
21. M. Patel, I. Mukhopadhyay, and A. Ray, *J. Alloys Compd.* 619, 458 (2015).
22. T. Řičica, L. Střižík, L. Dostál, M. Bouška, M. Vlček, L. Beneš, T. Wágner, and R. Jambor, *Appl. Organomet. Chem.* 29, 176 (2015).
23. K. Hosein, *Mater. Res. Express* 5, 046417 (2018).
24. H. Kafashan, *Mater. Sci. Semicond. Process.* 88, 148 (2018).
25. H. Kafashan, M. Azizieh, and Z. Balak, *Appl. Surf. Sci.* 410, 186 (2017).
26. H. Kafashan, M. Azizieh, and H. Nasiri Vatan, *J. Alloys Compd.* 686, 962 (2016).
27. H. Kafashan, and Z. Balak, *Spectrochim. Acta, Part A* 184, 151 (2017).
28. C. Gao, H. Shen, and L. Sun, *Appl. Surf. Sci.* 257, 6750 (2011).
29. H.Y. He, J. Fei, and J. Lu, *Mater. Sci. Semicond. Process.* 24, 90 (2014).
30. C. Gao and H. Shen, *Thin Solid Films* 520, 3523 (2012).
31. S. Gedi, V.R. Minnam Reddy, C. Park, J. Chan-Wook, and K.T. Ramakrishna Reddy, *Opt. Mater.* 42, 468 (2015).
32. A. Stadler, H.J. Schimper, U. Brendel, D. Topa, A. Basch, and H. Dittrich, *Thin Solid Films* 519, 7951 (2011).
33. L.L. Cheng, M.H. Liu, M.X. Wang, S.C. Wang, G.D. Wang, Q.Y. Zhou, and Z.Q. Chen, *J. Alloys Compd.* 545, 122 (2012).
34. W. Cai, J. Hu, Y. Zhao, H. Yang, J. Wang, and W. Xiang, *Adv. Powder Technol.* 23, 850 (2012).
35. F. Jiang, H. Shen, C. Gao, B. Liu, L. Lin, and Z. Shen, *Appl. Surf. Sci.* 257, 4901 (2011).
36. F. Zakerian, and H. Kafashan, *Superlattices Microstruct.* 124, 92 (2018).
37. A. Azmand, and H. Kafashan, *Ceram. Int.* 44, 17124 (2018).
38. T. Seymour, P. Frankel, L. Balogh, T. Ungár, S.P. Thompson, D. Jädernäs, J. Romero, L. Hallstadius, M.R. Daymond, G. Ribárik, and M. Preuss, *Acta Mater.* 126, 102 (2017).
39. T. Ungar, J. Gubicza, G. Ribarik, and A. Borbely, *J. Appl. Crystallogr.* 34, 298 (2001).
40. Z. Fan, B. Jóni, L. Xie, G. Ribárik, and T. Ungár, *J. Nucl. Mater.* 502, 301 (2018).
41. X. Chen, C. Dejoie, T. Jiang, C.-S. Ku, and N. Tamura, *MRS Bull.* 41, 445 (2016).
42. A.S. Budiman, G. Lee, M.J. Burek, D. Jang, S.M.J. Han, N. Tamura, M. Kunz, J.R. Greer, and T.Y. Tsui, *Mater. Sci. Eng., A* 538, 89 (2012).
43. I. Radchenko, S.K. Tippabhotla, N. Tamura, and A.S. Budiman, *J. Electron. Mater.* 45, 6222 (2016).
44. A. Davydok, T.W. Cornelius, C. Mocuta, E.C. Lima, E.B. Araujo, and O. Thomas, *Thin Solid Films* 603, 29 (2016).
45. X.M. Zeng, Z. Du, N. Tamura, Q. Liu, C.A. Schuh, and C.L. Gan, *Acta Mater.* 134, 257 (2017).
46. J. Kou, K. Chen, and N. Tamura, *Scripta Mater.* 143, 49 (2018).
47. N. Vaxelaire, S. Labat, T.W. Cornelius, C. Kirchlechner, J. Keckes, T. Schulli, and O. Thomas, *Acta Mater.* 78, 46 (2014).
48. R. Sivakami, S. Dhanuskodi, and R. Karvembu, *Spectrochim. Acta, Part A* 152, 43 (2016).
49. G.H. Khorrami, A. Khorsand Zak, A. Kompany, and R. Yousefi, *Ceram. Int.* 38, 5683 (2012).
50. A.S. Budiman, P.R. Besser, C.S. Hau-Riege, A. Marathe, Y.C. Joo, N. Tamura, J.R. Patel, and W.D. Nix, *J. Electron. Mater.* 38, 379 (2009).
51. A. Budiman, W. Nix, N. Tamura, B. Valek, K. Gadre, J. Maiz, R. Spolenak, and J. Patel, *Appl. Phys. Lett.* 88, 233515 (2006).
52. T.M.K. Thandavan, S.M.A. Gani, C. San Wong, and R.M. Nor, *J. Nondestr. Eval.* 34, 14 (2015).
53. J.-M. Zhang, Y. Zhang, K.-W. Xu, and V. Ji, *Solid State Commun.* 139, 87 (2006).
54. V. Biju, N. Sugathan, V. Vrinda, and S.L. Salini, *J. Mater. Sci.* 43, 1175 (2008).
55. J. Morales, E. Andrade, and M. Miki-Yoshida, *Thin Solid Films* 366, 16 (2000).
56. M. Devika, N.K. Reddy, K. Ramesh, K. Gunasekhar, E. Gopal, and K.R. Reddy, *J. Electrochem. Soc.* 153, G727 (2006).
57. K. Rogers and P. Daniels, *Biomaterials* 23, 2577 (2002).
58. J. Malleshappa, H. Nagabhushana, S.C. Sharma, D.V. Sunitha, N. Dhananjaya, C. Shivakumara, and B.M. Nagabhushana, *J. Alloys Compd.* 590, 131 (2014).
59. Y. Rosenberg, V.S. Machavariani, A. Voronel, S. Garber, A. Rubshtein, A. Frenkel, and E. Stern, *J. Phys.: Condens. Matter* 12, 8081 (2000).
60. P.K. Jisha, R. Naik, S.C. Prashantha, H. Nagabhushana, S.C. Sharma, H.P. Nagaswarupa, K.S. Anantharaju, B.D. Prasad, and H.B. Premkumar, *J. Lumin.* 163, 47 (2015).
61. G.K. Williamson and W.H. Hall, *Acta Metall.* 1, 22 (1953).
62. K.-C. Feng, Y.-H. Su, C.-C. Chou, Z.-M. Liu, and L.-W. Chu, *Chin. J. Phys.* 50, 932 (2012).
63. K. Reimann and R. Würschum, *J. Appl. Phys.* 81, 7186 (1997).
64. J.F. Nye, *Physical Properties of Crystals: Their Representation by Tensors and Matrices* (Oxford: Oxford University Press, 1985).
65. X. He, H. Shen, W. Wang, Z. Wang, B. Zhang, and X. Li, *J. Alloys Compd.* 556, 86 (2013).
66. K.A. Aly, N.M. Khalil, Y. Algamal, and Q.M.A. Saleem, *J. Alloys Compd.* 676, 606 (2016).
67. M.A. Tagliente and M. Massaro, *Nucl. Instrum. Methods Phys. Res., Sect. B* 266, 1055 (2008).
68. A. Khorsand Zak, W.H.A. Majid, M. Ebrahimizadeh Abrishami, R. Yousefi, and R. Parvizi, *Solid State Sci.* 14, 488 (2012).
69. Y.T. Prabhu, K.V. Rao, V.S.S. Kumar, and B.S. Kumari, *World J. Nano Sci. Eng.* 4, 21 (2014).
70. A. Khorsand Zak, W.H. Abd, M.E.Abrishami Majid, and R. Yousefi, *Solid State Sci.* 13, 251 (2011).
71. B. Choudhury and A. Choudhury, *Mater. Chem. Phys.* 131, 666 (2012).